IR spectroscopic characterization of 3d transition metal carbene cations, $FeCH_2^+$ and $CoCH_2^+$: Periodic Trends and A Challenge for DFT approaches

Frank J. Wensink,[1] Corry E. Smink,[1] P. B. Armentrout,[2] and Joost M. Bakker[1]

[1]*Radboud University, Institute for Molecules and Materials, FELIX Laboratory, Toernooiveld 7, 6525 ED Nijmegen, The Netherlands*
[2]*University of Utah, Department of Chemistry, 315 South 1400 East, Salt Lake City, Utah 84112, United States*

ABSTRACT

A combination of IR multiple-photon dissociation (IRMPD) action spectroscopy and quantum chemical calculations was employed to investigate the $[M,C,2H]^+$ (M = Fe and Co) species. These were formed by reacting laser ablated M^+ ions with oxirane (ethylene oxide, *c*-C_2H_4O) in a room temperature ion trap. IRMPD spectra for the Fe and Co are very similar and exhibit one major band. Comparison with density functional theory (DFT) and coupled cluster with single and double excitations (CCSD) calculations allow assignment of the spectra to MCH_2^+ carbene structures. For these 3d transition metal systems, experimental IRMPD spectra compare relatively poorly with DFT calculated IR spectra, but CCSD calculated spectra are a much better match primarily because the M-C stretch gains significant intensity. The origins of this behavior are explored in some detail. The present results are also compared to previous results for the 4d and 5d congeners and the periodic trends in these structures are evaluated.

INTRODUCTION

Research investigating the functionalization of the C–H bonds of alkanes has a long history.[1, 2] The bottleneck in making such a process both energy-efficient and selective is the activation of the strong C–H bonds. Methane is the most commonly studied alkane, largely because it is a major component of natural gas and the simplest alkane molecule. Selective C–H bond activation is particularly important because it is desirable to convert methane into liquid fuels like methanol that remain energy rich but are more easily transported. In general, the direct use of methane in catalytic processes is not presently pursued because the available processes are not sufficiently specific or energy efficient. Instead, the starting point is often thermal cracking, after which the available products are used to synthesize more valuable chemicals. The direct utilization of methane still requires the development of more effective C–H bond activation catalysts, especially those for earth abundant metals.

Potentially, studies of models systems of active catalyst sites provide a means to rationally design the needed catalysts. Model systems can provide a more detailed description of the fundamental interactions between methane and the active site,[3-5] allowing insight into how to manipulate the site for better efficiency and/or selectivity. Isolation of such model systems in the gas phase allows the most detailed information on the intrinsic interaction to be obtained as the perturbing effects of solvent or support are absent. Previous studies have found that several third-row (5d) transition metal (TM) cations, Ta^+, W^+, Os^+, Ir^+, and Pt^+, will activate methane at room temperature. These dehydrogenation reactions lead to formation of $[M,C,2H]^+$ products.[6-17] IR spectroscopic characterization of these $[M,C,2H]^+$ products showed that $[Ta,C,2H]^+$ and $[W,C,2H]^+$ have MCH_2^+ carbene structures but are unsymmetrical because of distortions induced by agostic interactions.[18-20] In contrast, $[Pt,C,2H]^+$ has a carbene structure with C_{2v} symmetry. Although Ir^+ also

exhibited experimental evidence for a symmetric $IrCH_2^+$ carbene structure, the main species formed for both $[Os,C,2H]^+$ and $[Ir,C,2H]^+$ was a hydrido metal carbyne $HMCH^+$.[18-21] Notably, the favored $HIrCH^+$ structure had been discarded on the basis of theoretical relative energies,[22] demonstrating the need for experimental spectroscopic characterization. In contrast to third-row TM cations, none of the first-row (3d) TM cations dehydrogenates methane exothermically,[15, 23-31] and although the second-row (4d) TM cations, Zr^+ and Nb^+ have been reported to dehydrogenate methane at room temperature,[15, 32, 33] guided ion beam studies demonstrate that such reactions are endothermic for all 4d TM cations. [28, 34-39] To understand the underlying reasons why the reactions of the lighter 3d TM cations with methane are unproductive and endothermic, it is of interest to characterize the structures of $[M,C,2H]^+$ products where M is a first-row TM.

Because Os^+ and Ir^+ were shown to be the most reactive 5d TM ions for methane dehydrogenation and also show the most diversity in their structures,[13, 16-19, 21] we have previously studied the bonding nature and structures of $[M,C,2H]^+$ with their second-row congeners: the elements of groups 8 and 9, M = Ru and Rh. The present study continues this examination of periodic trends by focusing on the first-row congeners, M = Fe and Co. Earlier studies investigated the M^+–CH_2 bond strengths for first-row TMs and found that the bond dissociation energy (BDE, D_0) decreased with an increase in the promotion energy (required for promoting a *d* electron to an *s* orbital) of the atomic metal cation.[40] The iron carbene cation BDE, $D_0(Fe^+–CH_2)$, was determined to be 3.53 ± 0.04 eV in guided ion beam tandem mass spectrometry (GIBMS) experiments[41, 42] and ≤3.54 ± 0.02 eV by photodissociation,[43] such that formation of $FeCH_2^+ + H_2$ from reaction with methane is endothermic by 1.21 ± 0.04 eV given $D_0(CH_2–H_2)$ = 4.743 ± 0.001 eV.[44] $D_0(Co^+–CH_2)$ was experimentally determined to be 3.29 ± 0.05 eV by GIBMS[30] and ≤3.43 ± 0.02 eV by photodissociation,[43] such that dehydrogenation of methane requires 1.46 ± 0.05 (≥1.31 ± 0.02) eV. In both

the iron and cobalt systems, the cross sections measured for the $M^+ + CH_4 \rightarrow [M,C,2H]^+ + H_2$ reactions had threshold energies that exceeded the endothermicities, clearly showing the presence of an energy barrier, which is more than likely found in the exit channel.[30, 42]

Elsewhere, CCSD calculations on the $[M,C,2H]^+$ species indicate that $FeCH_2^+$ has $^4B_1$ and $^4B_2$ electronic states that are nearly degenerate, similar to $CoCH_2^+$, which has nearly degenerate $^3A_1$ and $^3A_2$ electronic states.[45] A potential energy surface (PES) for reaction between Co^+ and CH_4 identified the physisorbed $Co(CH_4)^+$ complex as the only intermediate that could be formed exothermically along the surface leading toward $CoCH_2^+ + H_2$.[30, 46] A similar conclusion holds for the reaction between Fe^+ and CH_4.[42, 47]

Because neither Fe^+ nor Co^+ reacts exothermally with methane,[25, 30] we react the corresponding M^+ ions with oxirane (ethylene oxide, *c*-C_2H_4O) in order to form the $[M,C,2H]^+$ of interest. Oxirane readily reacts with many TM cations because of its ring strain and because $[M,C,2H]^+$ formation is accompanied by the stable CH_2O neutral product. As a consequence, extraction of CH_2 from oxirane requires much less energy than from methane, $D_0(CH_2–CH_2O) = 3.375 \pm 0.004$ eV, compared to $D_0(CH_2–H_2) = 4.743 \pm 0.001$ eV.[44] Thus, the thermochemistry noted above indicates that formation of $MCH_2^+ + CH_2O$ in the reaction of M^+ with oxirane, is exothermic by 0.16 ± 0.04 eV for M = Fe. For M = Co, the reaction is either slightly endothermic by 0.08 ± 0.05 eV or exothermic by $\leq 0.06 \pm 0.02$ eV. Indeed, the reaction of Fe^+ with oxirane has been shown to result in formation of both FeO^+ and $FeCH_2^+$ at thermal energies,[48] whereas Co^+ + oxirane results mainly in $CoCH_2^+$, $CoCO^+$, and $CoC_2H_4O^+$.[49] In that study, the kinetic energy dependence of the $CoCH_2^+$ cross section was consistent with a slightly endothermic process but the reaction is still appreciable (reaction efficiency near 10% at thermal energies).

In the present work, we probe the structure of the $[M,C,2H]^+$ product ions for M = Fe and

Co using a combination of infrared multiple photon dissociation (IRMPD) action spectroscopy and theoretical calculations. IRMPD spectra are recorded using the same Fourier transform ion cyclotron resonance (FTICR) mass spectrometer recently used to show that the reaction of Pt^+ with two methane molecules leads to the formation of a Pt^+(ethene) complex following two dehydrogenations and C–C coupling.[50] In that same work, we demonstrated that the spectrum of $[Pt,C,2H]^+$ recorded with this instrument is consistent with that reported previously,[18] where $[Pt,C,2H]^+$ was formed in a molecular beam environment without mass-isolation prior to irradiation. Earlier attempts to record IRMPD spectra of $[M,C,2H]^+$ with M = Fe and Co were unsuccessful in the molecular beam apparatus because the ion intensities were insufficient. Here, we take advantage of the possibility to react TM^+ with *c*-C_2H_4O over longer times and to mass-isolate the formed $[M,C,2H]^+$ species in order to obtain the desired spectra.

Critically, these small ions also form benchmark systems for the accuracy of the quantum chemical methods. Previously, we found that relatively standard density functional theory (DFT) methods proved sufficient to accurately predict the IR fingerprints, both in terms of frequencies and IR intensities, necessary for assigning the experimental IR spectra of $[M,C,2H]^+$ species with M 5d elements.[18-21, 50] For the 4d elements M = Ru and Rh, the same conclusion holds, even though the assignment for the $[Rh,C,2H]^+$ species was complicated by the multi-reference character of $RhCH_2^+$.[51] In contrast, here, we find that these comparisons are not so straightforward for 3d elements. We therefore employ higher-level methods to interpret the observed spectra.

METHODS

Experimental

The experimental procedure here mirrors that followed in our recent work on the similar

$[Ru,C,2H]^+$ and $[Rh,C,2H]^+$ species.[51] The atomic metal (Fe, Co) cations were formed by irradiating a solid metal target disk with a frequency doubled Nd:YAG laser at 30 Hz.[52, 53] Helium gas was injected by a pulsed valve in order to collisionally cool the metal ions and guide them to an orifice where the gas mixture adiabatically expanded into vacuum, further cooling all species. The ions were transferred by a radio-frequency (rf) only quadrupole mass filter, to a rf quadrupole ion trap having rectangular electrodes. There the ions were trapped by collisions with 5×10^{-4} mbar of argon buffer gas, which contained a partial pressure of 1×10^{-6} mbar of oxirane. After accumulating for approximately 400 ms, atomic metal cations and product ions were released from the trap by lowering the voltage on the exit electrode of the ion trap. The ions were then guided into one of four cells of the FTICR mass spectrometer integrated with the cavity of the Free Electron Laser for IntraCavity Experiments (FELICE). The first FTICR cell (cell 1) was located in the laser focus and the fourth was 30 cm from the focus, which reduces the photon fluence by a factor of 14. After ion capture, unwanted masses were ejected from the FTICR cell using a combination of chirped and single-frequency rf excitation pulses,[54] leaving only $[M,C,2H]^+$ ions. Resonant absorption of IR photons at a vibrational band of the ion increased the internal energy of the ions leading to fragmentation. IRMPD spectra were recorded by monitoring intensities of precursor (I_p) and fragment (I_{frag}) ions present in the FTICR cell after irradiation. The resulting spectrum is provided as the fragmentation yield *Y:*

$$Y = \ln\left(\frac{I_p + I_{frag}}{I_p}\right)$$

The IR light of FELICE was scanned over the 300 – 2000 cm^{-1} spectral range for the present work. FELICE produced micropulses at 1 GHz, with macropulses that lasted between 6 – 10 μs at a repetition rate of either 5 or 10 Hz. A single macropulse with the ions in FTICR cell 4 (low fluence) was used to record all spectra unless indicated otherwise. Macropulse energies of FELICE

ranged from 0.3 to 0.5 J moving from low to high frequencies. This corresponds to macropulse fluences ranging from 0.9 to 6.6 J/cm^2 in FTICR cell 4. The spectral bandwidth was near transform limited and the full-width at half-maximum (FWHM) was approximately 0.7% of the central frequency during the present experiments. To locate the band frequencies listed below, Gaussian curves were fitted to the experimental IRMPD spectra.

Computational

All calculations were performed here using the Gaussian 16 software package.[55] Generally, molecular structures for all species were located using unrestricted B3LYP hybrid functional and the def2-TZVPPD basis set, which treats all electrons explicitly for H, C, Fe, and Co.[56-58] This combination was used because it has performed well in calculating the IR spectra of the 5d $[M,C,2H]^+$ species and the M^+–CH_2 BDEs calculated at this level match experimental values relatively well: $D_0(Fe^+–CH_2)$ was calculated to be 3.66 eV (experimentally 3.53 ± 0.04 eV) and $D_0(Co^+–CH_2)$ = 3.24 eV (3.29 ± 0.05 eV), as outlined in Table 1. These calculated values (as well as all others provided below) include zero-point vibrational energies. True minima in the structures were verified by ensuring that the calculated harmonic vibrational frequencies were all real. For comparison with the experimental spectra, the unscaled theoretical harmonic vibrational frequencies had simulated rovibrational envelopes included by assuming pure *a*-, *b*-, or *c*-type transitions.[59] To mimic the FELICE spectral bandwidth, the resulting rovibrational transition lines were convolved with a Gaussian line shape having a FWHM of 0.9% of the central frequency. To simulate additional broadening effects, convolutions were also done employing a 9% FWHM bandwidth.

Additional geometry and frequency calculations were done at second-order Møller-Plesset,

MP2(full),[60] and coupled cluster with single and double excitations, CCSD(full),[61] levels (where full indicates correlation of all explicit electrons) using the same def2-TZVPPD basis set. These were followed by single point calculations with added perturbative triple excitations, i.e., at the CCSD(T,full) level. For $FeCH_2^+$, calculations using several additional DFT approaches were also pursued.

Notably, no scaling factors were used to compare the theoretical spectra with experiment, which is unusual for these types of systems.[18-21, 50, 51, 62-64] Nevertheless, such scaling factors were not found to improve the agreement between theory and experiment and therefore are not used throughout this work.

RESULTS & DISCUSSION

Reactions between M^+ (M = Fe, Co) and oxirane resulted in the product mass distributions shown in Figure S1 of the Supporting Information. We observed ionic products $[M,C,2H]^+$, MO^+, $[M,O,H]^+$, and $[M,O,2H]^+$ for both M. For Fe^+, the former two products were observed in earlier experiments,[48] but the latter two were not. We assume these species are the result of reaction with a water contaminant present in the *c*-C_2H_4O gas or tubing. In the reaction between Co^+ and oxirane, we do observe $[Co,C,2H]^+$ and CoO^+ but not the $CoCO^+$ species observed before in a single bimolecular encounter.[49] We also observe a $[Co,C,3H]^+$ species (which would not have been observed easily in the low mass resolution ion beam experiments). Formation of $CoCH_3^+$ + HCO from Co^+ + *c*-C_2H_4O is endothermic by 0.29 ± 0.04 eV.[41] The absence or presence of these species might be a result of multiple reactions with *c*-C_2H_4O or involve electronic excitation of Co^+. Observed $[Co,O,2H]^+$ and $[Co,O,H]^+$ species again are likely to result from reactions with a water contaminant.

IR spectroscopy of $FeCH_2^+$

Figure 1a shows the experimental IRMPD spectrum of $[Fe,C,2H]^+$ (*m/z* = 70) constructed using the ^{56}Fe isotope of the two observed fragment masses Fe^+ and FeC^+. The spectrum is dominated by a strong and broad band peaking at 632 cm^{-1}. This band has a shoulder on the high frequency side with a maximum near 767 cm^{-1}. Figure S2a of the Supporting Information shows a potential band could be discerned in only the Fe^+ fragmentation channel just above 1000 cm^{-1}. A careful analysis of the mass-spectra underlying the IR spectra shows that this band results from formation of Fe^+ by fragmentation of a $[Fe,C,3H]^+$ minor product that was not mass-eliminated before irradiation, see a typical example in Figure S3 in the Supporting Information. As $[Fe,C,3H]^+$ does not dissociate by loss of H_2 + H, this band does *not* appear in the FeC^+ fragmentation product spectrum. A second band for $[Fe,C,3H]^+$ is observed to coincide with the main band of $[Fe,C,2H]^+$, and therefore has no influence on the current spectrum because of the low intensity of the $[Fe,C,3H]^+$ product.

When fragmentation occurred, up to 50% of the original $[Fe,C,2H]^+$ intensity was retained, and the yield of Fe^+ was roughly twice that of FeC^+, as shown in Figure S2a of the Supporting Information. This observation appears at odds with the calculated dissociation energies for the fragmentation channels of $[M,C,2H]^+$ listed in Table 1, which indicate that formation of FeC^+ and H_2 is thermodynamically preferred. However, formation of $Fe^+ + CH_2$ requires direct cleavage of the Fe–C bond over a loose transition state (TS), whereas formation of $FeC^+ + H_2$ is more complicated as it requires cleavage of both C–H bonds and formation of the H_2 bond, and thus likely involves a tight TS. Such a tight TS would make the latter process entropically less favorable, and further, it potentially could result in a barrier in excess of the endothermicity shown in Table 1.

The calculated ground state (GS) for $[Fe,C,2H]^+$ is a C_{2v} symmetric iron carbene geometry, $FeCH_2^+$, with a $^4B_1$ electronic state and a covalent double bond between the metal and CH_2 group. Note that formation of this quartet spin species would require a spin surface crossing if the reactant Fe^+ ions were efficiently cooled to their ^6D ground state; however, it is also possible that the laser ablation source creates a population of the low-lying ^4F excited state of Fe^+. With the convention that the z-axis is the symmetry axis and that the molecule lies in the yz plane, the $^4B_1$ GS has a Fe-C σ bonding molecular orbital (MO) (a_1 symmetry, using $3d_{z2}$ on Fe, double occupancy), a Fe–C π bond (b_1, Fe $3d_{xz}$, double), three non-bonding MOs localized on Fe: (a_1, $3d_{x2-y2}$, double; a_2, $3d_{xy}$, single; a_1, 4s, single), and an antibonding MO combining the Fe $3d_{yz}$ and CH_2 orbitals (b_2, single). Thus, the valence MO occupation (excluding the four CH_2 bonding electrons) is $(1a_1)^2(1b_1)^2(2a_1)^2(1a_2)^1(3a_1)^1(1b_2)^1$.

Several additional electronic states were found on the quartet spin surface that also have the symmetric C_{2v} structure. A second electronic state, $^4B_2$, calculated to lie only 0.013 eV higher in energy, reverses the occupation of the $3d_{x2-y2}$ ($2a_1$) and $3d_{xy}$ ($1a_2$) MOs; their non-bonding character explains the small energy difference between these two states. In another low-lying state ($^4A_2$), one electron in the $3d_{x2-y2}$ ($2a_1$) MO is transferred to the antibonding $1b_2$ MO, leading to decreased stability, 0.18 eV above the GS. Additional carbene structures were located for different spin states. A $^6B_1$ state located 0.83 above the GS has a MO occupation of $(1a_1)^2(1b_1)^1(2a_1)^2(1a_2)^1(3a_1)^1(1b_2)^1(2b_1)^1$ where the $2b_1$ MO is the antibonding version of the $1b_1$ Fe–C π bond. Two carbene structures were found on the doublet surface, of which the lowest, $^2A''$ has the same electron configuration as the $^4B_1$ ground state, $(1a_1)^2(1b_1)^2(2a_1)^2(1a_2)^1(3a_1)^1(1b_2)^1$, but is slightly distorted from C_{2v} symmetry (although the MOs can still be labeled using this symmetry) with Fe–H distances of 2.52 and 2.58 Å. This state lies 1.04 eV above the GS. The second

doublet state located, a $^2A_2$ $(1a_1)^2(1b_1)^2(2a_1)^2(1a_2)^1(3a_1)^0(1b_2)^2$ state with C_{2v} symmetry, lies only 0.02 eV above the ^{2}A" state. A summary of all structures and electronic states, including energies relative to the reactants, found in this study is presented in the Supporting Information, Table S1.

We also explicitly checked whether stable agostic iron carbene geometries could be located, but as there are no empty 3d orbitals on Fe^+, these all converged to symmetric carbene geometries. We did find a hydrido iron carbyne structure, $HFeCH^+$ but only on the sextet surface (^{6}A") lying 3.32 eV above the GS. The lowest energy species with both hydrogen atoms connected to iron is a dihydrogen iron carbide, $(H_2)FeC^+$ (^{2}A') at 2.70 eV. Here, the H–H bond distance of 0.787 Å is slightly longer than the 0.743 Å calculated here at the same level of theory for the free H_2 molecule. A dihydrido iron carbide, H_2FeC^+ (H–H distance is 2.88 Å) in a ^{4}A" state was found 5.54 eV above the GS.

Figure 1b-h shows the simulated IR spectra of different $[Fe,C,2H]^+$ isomers and states located computationally. Many species shown have calculated vibrational modes near the experimental bands. Of the six fundamental vibrations of C_{2v} metal carbenes, two correspond to the symmetric and antisymmetric C–H stretch vibrations and are calculated to lie near 3100 cm^{-1}. Four modes are located somewhere between 500 and 1500 cm^{-1}: the CH_2 rocking mode (in-plane CH_2 bend, b_2 symmetry, *b*-type transition), the M–C stretch (a_1, *a*-type), the CH_2 wagging mode (out-of-plane CH_2 bend, b_1, *c*-type), and the CH_2 scissoring mode (a_1, *a*-type). For the $FeCH_2^+$ ($^4B_1$) GS structure, these modes are calculated at 554, 627, 787, and 1321 cm^{-1}, respectively, Table 2, with the C-H stretches at 3078 and 3182 cm^{-1}. According to B3LYP calculations, the CH_2 wagging and rocking vibrations are most intense (36 and 101 km/mol), whereas the Fe-C stretch and CH_2 scissoring mode (both involving *a*-type transitions) have calculated intensities of only 5 and 1 km/mol, respectively. The effects of varying the MO occupation on the calculated IR spectrum are only

marginal, with the main difference being a shift of the CH_2 out-of-plane wagging vibration from 787 cm^{-1} ($^4B_1$ GS) to 716 cm^{-1} ($^4B_2$), Table 2.

The rotational profile simulations for all species in Figure 1 reflect the large rotational constants involved (e.g., 9.98, 0.39, and 0.38 cm^{-1} for the $^4B_1$ GS), which, in combination with the room temperature conditions of the experiment, lead to broad bands with complex substructure. The exothermicity of the reaction of Fe^+ with oxirane is 0.16 ± 0.04 eV, indicating that the three lowest energy states are accessible at thermal energies (and potentially others if appreciable electronic excitation were retained by Fe^+). Indeed, the energy difference between the $^4B_1$ and $^4B_2$ states is so small that population of both states is reasonable. Nevertheless, none of the three low-energy species in panels b-d yields a very convincing match with the experiment, although for all three structures, a broad absorption is predicted with the center of gravity close to the center of the experimentally observed band.

Comparison between simulated spectra for higher energy species and the experimental spectrum does not offer reason to suspect their presence. The $^6B_1$ structure at +0.83 eV has a significantly different IR spectrum, most notably from the intensity increase of the CH_2 scissoring mode to 58 km/mol, while the CH_2 wagging mode massively red shifts to 142 cm^{-1} and is left with an intensity of 14 km/mol. The only spectrum that shows a compact band structure is that calculated for the $^2A_2$ species, which arguably resembles the experimental spectrum best in shape but is shifted to the blue; it is, however, difficult to see how the formation of a structure at more than 1 eV above the GS could be favored, especially given the number of spin crossings required for its formation.

Alternative levels of theory for the spectroscopy of $FeCH_2^+$

Because of the mismatch in the comparison of the B3LYP computational spectra with experiment, we also explored other levels of theory, starting with MP2. The MP2 calculation of the $^4B_1$ state provided similar vibrational frequencies as the B3LYP calculation, 593, 660, 710, 1409, 3160, and 3273 cm^{-1}, but to our surprise, the intensity profile was substantially different, primarily because the intensities of the two *a*-type transitions were much higher, 76 and 34 km/mol, respectively, versus 5 and 1 km/mol for B3LYP (see Figure S4). The enhanced intensity of the Fe-C stretch would be sufficient to better reproduce the experimental band, whereas the enhanced intensity of the CH_2 scissors mode is inconsistent with the failure to observe a band in this wavenumber range. To explore this phenomenon further, we performed CCSD/def2-TZVPPD calculations. CCSD(T)//CCSD calculations place the $^4B_2$ state only 0.0005 eV above the $^4B_1$ GS. CCSD geometry optimizations for the $^4B_1/^4B_2$ states provide similar frequency predictions as the B3LYP results, 570/567, 647/646, 754/744, 1358/1359, 3122/3122, and 3228/3227 cm^{-1}, but again the intensity profile is distinct. Now, the CH_2 rock (*b*-type) and wag (*c*-type) have similar intensities (45/50 and 106/98, respectively), whereas the *a*-type Fe-C stretch has a much larger predicted intensity (43/43 km/mol) compared to the B3LYP results. Unlike the MP2 results, the scissors (*a*-type) mode has an intensity (<1/<1 km/mol) consistent with experiment. Figure 2 compares the CCSD predicted spectrum for the $^4B_1$ GS (the $^4B_2$ spectrum is very similar, see Figure S5b of the Supporting Information) with the experimental spectrum and clearly provides an improved match compared with the B3LYP results of Figure 1. Figure 2 also includes a predicted spectrum with the Fe-C stretch band having an intensity that matches the MP2 calculation. As shown in Figure 2c that includes more broadening, the latter is probably the best match to the experimentally observed band. It can also be realized that some of variations in intensities may be a result of comparing the multiple photon experimental absorptions with the single photon theoretical predictions.

The enhanced intensity in the Fe-C stretch in both MP2 and CCSD computations is the result of a well-known phenomenon in DFT calculations,[65-68] which generally underestimate the charge separation in something like the Fe-CH_2 bond and therefore the dipole derivative with respect to the Fe-C stretch. For instance, in the $^4B_1$ ground state, the charges on Fe and CH_2 calculated at the equilibrium geometry using B3LYP are +1.16 e and -0.16 e, respectively, (for a charge difference of 1.32 e), but +1.51 e and -0.51 e for CCSD (charge difference of 2.01 e). As the bond extends by 0.2 Å, the charge difference changes by +0.02 e for B3LYP (leading to very low IR intensity) but by -0.15 e for CCSD (yielding a moderate IR intensity). This phenomenon was explored further by examining results for several other density functionals,[56, 57, 69-80] as detailed in Table 3. In general, all DFT approaches show the same trends with the predicted intensity of the Fe-C stretch varying from 3 – 24 km/mol, while maintaining the CH_2 wag at 96 – 109 km/mol (except M06-2X at 83 km/mol). All of these lie less than about half the intensity found at the CCSD level. The predicted frequency for the Fe-C stretch is insensitive to the level of theory, varying from 619 to 675 cm^{-1}, which indicates that the different levels of theory yield similar force constants for this motion. In contrast, the CH_2 wag shows modest dispersion, 678 – 808 cm^{-1}. This is shown pictorially in Figure 3 for all four modes accessible in the present experiment. The Fe-C stretch shows the largest range of intensities with the DFT values clustered at low values, CCSD being intermediate, and MP2 relatively high. The CH_2 wags have comparable intensities for all levels of theory. The dispersion in intensities is also generally small for the CH_2 rock and scissors motions. Here, the outliers for the CH_2 rock are MN15L (1 km/mol) and TPSS (24 km/mol), with all other levels of theory clustered between 36 and 55 km/mol. Note that these two levels also predict frequencies much lower than other levels. For the CH_2 scissors, the outliers are MP2 harmonic (34 km/mol) and anharmonic (44 km/mol) with all other levels of theory, including CCSD,

predicting a very weak band intensity. Here, most levels of theory predict a frequency between 1313 and 1358 cm^{-1}, whereas the MP2 calculations shift this up by more than 50 cm^{-1}. Because of the disparity in the predicted intensities of the M-C stretch, we treat its intensity as a potential adjustable parameter in further comparisons between theory and experiment. The experimentally observed band positions, together with harmonic normal mode frequencies and intensities calculated at the B3LYP and CCSD levels are combined in Table 2.

IR spectroscopy of $CoCH_2^+$

Resonant IR irradiation of $[Co,C,2H]^+$ (*m/z* = 73) leads to two photofragments, Co^+ and CoC^+, with Co^+ being the major fragment (~90%), as shown in Figure S2b of the Supporting Information. This result is consistent with the thermochemistry in Table 1. Similar to the Fe case, the calculated dissociation energies for the fragmentation channels of $[Co,C,2H]^+$ listed in Table 1 slightly favor formation of CoC^+ and H_2. As discussed above, the observation that Co-CH_2 cleavage dominates may be because dehydrogenation is entropically less favorable and could have a barrier in excess of the endothermicity shown in Table 1.

Figure 4a shows the experimental IRMPD spectrum of $[Co,C,2H]^+$. It shows one dominant band, which appears to consist of two maxima around 673 and 811 cm^{-1}. The band has a relatively long tail to the blue which could be a third, weaker band. Its center is estimated around 948 cm^{-1}. Figure 4b-g shows the B3LYP simulated IR spectra of different $[Co,C,2H]^+$ isomers and states. The ground state is a symmetric cobalt carbene geometry, $CoCH_2^+$, with a $^3A_2$ electronic state. The MOs are the same as for $FeCH_2^+$, such that the valence MO configuration for the $^3A_2$ state is $(1a_1)^2(1b_1)^2(2a_1)^2(1a_2)^1(3a_1)^1(1b_2)^2$, with the singly occupied MOs being the $3d_{xy}$ ($1a_2$) and 4s ($3a_1$) MOs. A $^3A_1$ state, only 0.050 eV higher in energy, is obtained by moving an electron from the

$3d_{x2-y2}$ ($2a_1$) MO to the $3d_{xy}$ ($1a_2$) MO, both non-bonding. Thus, the $^3A_2$ and $^3A_1$ states of $CoCH_2^+$ are analogous to the $^4B_1$ and $^4B_2$ states of $FeCH_2^+$ with addition of the extra electron to the anti-bonding $1b_2$ MO. If the $1b_2$ MO is singly occupied instead of the $3a_1$ or $1a_2$ MOs, $^3B_1$ and $^3B_2$ states are found and lie 0.41 and 0.90 eV above the GS. Singlet spin states of $CoCH_2^+$ ($^1A_1$ and $^1A_2$) were found 0.71 and 0.77 eV above the GS. These states have the same valence MO configuration as the triplet states, but the two singly occupied MOs are singlet coupled instead of triplet coupled, leading to the higher energy. Similar to $[Fe,C,2H]^+$, trial structures for agostic cobalt carbenes collapsed into the symmetric carbenes, again because there are no empty 3d orbitals to support this distorted structure. The lowest energy quintet spin species is a distorted carbene with a $^5A'$ state found at 0.86 eV with one of the hydrogen atoms closer to the cobalt atom (2.56 and 2.63 Å). A second quintet carbene ($^5A''$) was found 0.94 eV above the GS and has both hydrogen atoms bent slightly out of the molecular plane (H–H–Co–C dihedral angle of 7.3°). The lowest-energy hydrido cobalt carbyne, $HCoCH^+$, was found on the quintet surface ($^5A'$) at 3.26 eV above the GS. All geometries with two hydrogens bound to cobalt converged to dihydrogen cobalt carbides, $(H_2)CoC^+$, with the lowest being a $^1A'$ state with an energy 3.09 eV above the GS. Table S1 of the Supporting Information lists all $[Co,C,2H]^+$ species located theoretically.

In contrast to the spectra calculated for Fe carbene isomers, those for cobalt carbene states are very much alike. As for the analogous $FeCH_2^+$ states, the $^3A_2$ and $^3A_1$ states of $CoCH_2^+$ shift the CH_2 rocking frequency, from 622 to 601 cm^{-1}, respectively, and the CH_2 wagging mode, from 877 to 893 cm^{-1}. The intensities of the CH_2 rocking and CH_2 wagging modes differ by at most 16%. The Co–C stretch and CH_2 scissoring modes both shift less than 5 cm^{-1} and have intensities below 3 km/mol in B3LYP calculations. Like the $FeCH_2^+$ results, the B3LYP spectra do not pro-

vide a good reproduction of the experimental spectrum for any structure located theoretically, Figure 4.

Therefore, we again tested MP2 and CCSD approaches. Similar to $FeCH_2^+$, the intensity profile obtained from MP2 calculations (Figure S4) greatly enhances the Co-C stretch, such that it is slightly *more* intense than the CH_2 out-of-plane wag (intensities of 76 and 83 km/mol for the $^3A_2$ and $^3A_1$ states, respectively). CCSD(T)//CCSD calculations indicate that the $^3A_1$ state lies only 0.015 eV above the $^3A_2$ GS. Figure 5 shows the spectrum predicted by the CCSD level of theory for the $^3A_2$ GS, where the Co-C stretch has a predicted intensity of 25 km/mol (the spectrum for the low-lying $^3A_1$ state is very similar as shown in Figure S5d of the Supporting Information). As for the case of $FeCH_2^+$, the experimental spectrum is matched better if the intensity of this band is approximately twice that predicted at the CCSD level. Here, the moderate IR intensity (23 km/mol) predicted for the CH_2 scissor vibration is not matched by the observed spectrum. In any case, we attribute the experimental spectrum to a combination of the symmetric cobalt carbene cation in both the closely-spaced $^3A_2$ and $^3A_1$ states because the reaction of ground state Co^+ (^3F, $3d^8$) with oxirane is slightly endothermic, by 0.08 ± 0.05 eV. Thus, formation of these states can be driven by near-thermal energies, as shown previously.[48] Although contributions from electronically excited states could be present, the lowest energy excited state of Co^+, ^5D ($4s^13d^7$), should be less reactive than the ^3F ($3d^8$) GS because the 4s orbital is occupied.[81]

Clearly, although the CCSD level reproduces the experimental spectrum with reasonable fidelity in the 500 – 1200 cm^{-1} range, the predicted peak near 1400 cm^{-1} (CH_2 scissors) is not found in the experimental spectrum. When irradiating $[Co,C,2H]^+$ under higher IR fluences (not shown), we observed a broad, unresolved band stretching from 500 – 1800 cm^{-1}. We speculate that under the current experimental conditions, IR excitation is not efficient enough to induce fragmentation

at the predicted 1400 cm^{-1} band and that higher intensities rapidly lead to non-resonant absorption.

Group 8 and 9 trends: Carbene verses hydrido carbyne

In previous work, we have presented the experimental IRMPD spectra of $[Ru,C,2H]^+$, $[Rh,C,2H]^+$,[51] $[Os,C,2H]^+$, and $[Ir,C,2H]^+$,[18-21] the 4d and 5d congeners of the group 8 and 9 species presented in this study. If we put the current assignments for Fe and Co in perspective with the previous findings, we note that both 5d elements (Os and Ir) prefer the formation of a hydrido carbyne structure, whereas the 3d elements form carbene structures. Our recent work showed that the 4d elements are mixed, with Ru forming both structures and Rh yielding only the carbene.[51] Energetically, 5d hydrido carbynes are preferred, but more strongly so for the group 8 elements as indicated by the energetics presented in Figure 6. This is consistent with the assignment of the product of osmium (a group 8 element) to $HOsCH^+$ ($^2A'$), whereas part of the product for iridium (group 9) is assigned to a carbene structure (0.3 eV higher in energy). This trend appears to hold for 4d elements, where the $^4B_2$ ruthenium carbene is almost isoenergetic with the $^2A'$ hydrido ruthenium carbyne, whereas the $HRhCH^+$ ($^1A'$) is significantly higher in energy than the $RhCH_2^+$ ($^1A_1$). For 3d elements, hydrido carbyne structures are not competitive at all, lying several eV higher in energy. Thus, as one moves down a group in the periodic table, hydrido carbyne structures become increasingly competitive in terms of energy compared to carbene structures, but less so along a row.

One rationale for these trends is thermodynamic. $H\text{-}M{\equiv}CH^+$ has four covalent bonds to the metal whereas MCH_2^+ only has two covalent M=C bonds. In general, the 5d TM have stronger bonds to C and H than the 4d or 3d TM, e.g., for group 9, see Figure 4 in ref. [13] (for group 8, see references [16, 39, 41, 43, 82-84]). Thus, the more highly coordinated hydrido carbyne structure becomes

more favorable for 5d relative to 4d TMs and even more so for 3d TMs. In addition, one can also consider the promotion energies required to put the metal cation into an electronic configuration needed for bonding. (Here, the promotion energies are averaged over all spin-orbit levels and taken from ref. [85].) For the group 8 elements, both MCH_2^+ and $HMCH^+$ species correlate with an (n-1)d^6ns^1 electronic configuration on M^+ so the thermodynamic considerations dictate the vertical trends. For the group 9 elements, the triplet states of MCH_2^+ correlate with the (n-1)d^7ns^1 electronic configuration on M^+. This is the ground state (GS) for Ir^+, a low-lying state for Co^+ (0.43 eV above the ^5F, $3d^8$ GS), but a high-energy state for Rh^+, 2.13 eV higher in energy than the ^5F ($4d^8$) GS. Thus, the $RhCH_2^+$ prefers the $^1A_1$ state that correlates with the ^5F ($4d^8$) GS. For the $HMCH^+$ structures of the group 9 elements, the $^1A'$ GS correlates with either an (n-1)d^6ns^2 or low-spin (n-1)d^7ns^1 (^3F) electronic configuration on M^+. The former configuration is generally higher in energy, whereas the latter lies 1.21, 3.13, and 1.33 eV above the GS of Co^+, Rh^+, and Ir^+, respectively. Because these promotion energies are much higher than those for the group 8 metal cations, the $HMCH^+$ structures are more favorable for group 8 than for group 9, as seen in Figure 6.

Figure 6 shows that the hydrido carbyne structures for 4d and 5d elements are found on the same or a lower spin surface as that of the lowest energy carbene structure. However, for Fe and Co, the lowest energy hydrido carbynes were found on the sextet and quintet spin surfaces, respectively. To investigate whether we might have missed carbyne structures on the lower spin surfaces, the potential energy surfaces (PESs) connecting the MCH_2^+ and $HMCH^+$ structures were calculated for both metal cations investigated in this study (Figure 7). PESs were generated by starting from a symmetric carbene structure and systematically increasing the C–M–H angle while the rest of the molecule was allowed to relax. The PES scans were generated for both the A' and A" con-

figurations in dashed and solid lines, respectively. No stable minimum for a hydrido carbyne structure for Fe or Co is found on any of the two lowest spin surfaces, explaining why all trial hydrido carbyne geometries for $[Fe,C,2H]^+$ and $[Co,C,2H]^+$ converged into the carbene structure. For Co, a very shallow well was located along the $^1A'$ surface, but this species is 3.7 eV above the symmetric cobalt carbene ground state.

Group 8 and 9 trends: Charge separation

The observation that the intensities of the M-C stretches of $FeCH_2^+$ and $CoCH_2^+$ are not predicted well at DFT levels of theory leads one to wonder how extensive this particular problem is. As noted above, our work with the 5d TM systems utilized B3LYP calculations that reproduced the experimental spectra with fidelity. Likewise, our recent studies of $[Ru,C,2H]^+$ showed comparable predictions between B3LYP and CCSD levels of theory.[51] For $[Rh,C,2H]^+$, the situation was complicated by the multireference character of the $RhCH_2^+$ states such that more advanced CCSD methods supplied the best reproduction of the data. Here, we directly compare the B3LYP and CCSD predictions for the group 8 and 9 transition metals to see how pervasive the problem is. We find that for the $^4B_1$ states of the group 8 carbenes, the only mode that changes intensity drastically (factor of 8 or more) is the M-C stretch for $FeCH_2^+$. For both $RuCH_2^+$ and $OsCH_2^+$, the intensity of the M-C stretch remains very small. For the group 9 carbenes in the $^3A_2$ state, $CoCH_2^+$ shows a dramatic increase in intensity for the M-C stretch and a more modest increase for the CH_2 scissors, whereas for $RhCH_2^+$ and $IrCH_2^+$, the M-C stretch intensities are comparable for B3LYP and CCSD calculations and the CH_2 scissors changes by factors of less than three. The results are summarized in Table S5 of the Supporting Information. Thus, the failure of DFT in predicting the intensities of the M-C stretch appears to be confined to the first-row (3d) TM.

CONCLUSION

Reacting the 3d group 8 and 9 transition metal ions (M^+ = Fe^+ and Co^+) with oxirane in a room temperature ion trap led to the formation of $[M,C,2H]^+$. These species were mass isolated in the FTICR mass spectrometer coupled to the infrared intracavity free-electron laser FELICE, where they were spectroscopically characterized. The IRMPD spectra of $[M,C,2H]^+$ with M = Fe and Co each contain one broad band around 700 cm^{-1} with minor differences in the extent of substructure. On the basis of B3LYP and CCSD(T)//CCSD energetics, both structures are expected to be carbenes. Comparison of the experimental IRMPD spectra with the predictions from DFT calculations offer poor agreement, making the assignment of structures tenuous at best. Calculations at the CCSD level offer a large improvement in the predicted intensities for the M–C stretch vibrations that match the experimental spectrum much better, although for $CoCH_2^+$, a simultaneous increase in the CH_2 scissor mode intensity is not matched by experiment. Nevertheless, these calculations suggest the structures of $[M,C,2H]^+$ for M = Fe and Co are indeed carbenes, each in two nearly degenerate electronic states.

The experimental spectra for $[Fe,C,2H]^+$ and $[Co,C,2H]^+$ are reproduced much better by CCSD calculations than by B3LYP calculations, primarily because the predicted intensity of the M-C stretch is much higher according to CCSD calculations. Indeed, enhanced M-C stretch intensities (consistent with MP2 calculations) provide even better agreement with experiment. This failure of the B3LYP functional appears to be systematic for all DFT approaches, although some functionals yield improved intensities but still do not match the CCSD predictions. This appears to be a consequence of a reduced separation in charge in the MCH_2^+ species. Exploration of this effect as one moves down the periodic table indicates that this failure does not propagate from the

3d TM to the 4d and 5d TM, where DFT approaches provide spectra that are in good agreement with experiment. Further, we explore the relative stabilities of the MCH_2^+ versus $HMCH^+$ species in terms of the periodic trends for these group 8 and 9 transition metals: Fe, Ru, Os and Co, Rh, Ir. It appears that promotion energy arguments are involved coupled with the number and strength of the covalent bonds needed to form the two structures.

ACKNOWLEDGMENTS

This work was funded by NWO's Materials for Sustainability program (grant no. 739.017.008). We gratefully acknowledge the Nederlandse Organisatie voor Wetenschappelijk Onderzoek (NWO) for the support of the FELIX Laboratory and for CPU time on the Dutch National Super-computers Cartesius and Snellius (project number 2021.055). Financial support was also provided by the National Science Foundation (grant no. CHE-2313553).

SUPPORTING INFORMATION

Figures showing the mass spectrum for reaction of Fe^+ and Co^+ with oxirane, branching ratios for the photofragmentation of $[Fe,C,2H]^+$ and $[Co,C,2H]^+$, comparisons of the experimental spectrum of $[Fe,C,2H]^+$ and $[Co,C,2H]^+$ to spectra calculated at the MP2(full)/def2-TZVPPD and CCSD/def2-TZVPPD levels. Tables provide details regarding the calculated states of $[M,C,2H]^+$ and relative intensities of vibrational bands for group 8 and 9 metal carbene cations.

REFERENCES

1. Crabtree, R. H. Organometallic alkane CH activation. *J. Organomet. Chem.* **2004,** *689*, 4083-4091.
2. Stone, K. L.; Borovik, A. S. Lessons from Nature: Unraveling Biological C–H Bond Activation. *Curr. Opin. Chem. Biol.* **2009,** *13*, 114–118.
3. Bohme, D. K.; Schwarz, H. Gas-Phase Catalysis by Atomic and Cluster Metal Ions: The Ultimate Single-Site Catalysts. *Angew. Chem. Int. Ed.* **2005,** *44*, 2336 – 2354.
4. Roithová, J.; Schröder, D. Selective Activation of Alkanes by Gas-Phase Metal Ions. *Chem. Rev.* **2010,** *110*, 1170–1211.
5. Sauer, J.; Freund, H. J. Models in Catalysis. *Catal. Lett.* **2015,** *145*, 109–125.
6. Buckner, S. W.; MacMahon, T. J.; Byrd, G. D.; Freiser, B. S. Gas-Phase Reactions of Nb^+ and Ta^+ with Alkanes and Alkenes. C-H Bond Activation and Ligand-Coupling Mechanisms. *Inorg. Chem.* **1989,** *28*, 3511-3518.
7. Irikura, K. K.; Beauchamp, J. L. Osmium Tetroxide and Its Fragment Ions in the Gas Phase: Reactivity with Hydrocarbons and Small Molecules. *J. Am. Chem. Soc.* **1989,** *111*, 75-85.
8. Irikura, K. K.; Beauchamp, J. L. Electronic Structure Considerations for Methane Activation by Third-row Transition-metal Ions. *J. Phys. Chem.* **1991,** *95*, 8344-8351.
9. Irikura, K. K.; Beauchamp, J. L. Methane Oligomerization in the Gas Phase by Third-Row Transition-Metal Ions. *J. Am. Chem. Soc.* **1991,** *113*, 2769-2770.
10. Achatz, U.; Beyer, M.; Joos, S.; Fox, B. S.; Niedner-Schatteburg, G.; Bondybey, V. E. The Platinum Hydrido-Methyl Complex: A Frozen Reaction Intermediate? *J. Phys. Chem. A* **1999,** *103*, 8200-8206.
11. Zhang, X.-G.; Liyanage, R.; Armentrout, P. B. The Potential Energy Surface for Activation of Methane by Pt^+: A Detailed Guided-Ion Beam Study. *J. Am. Chem. Soc.* **2001,** *123*, 5563-5575.
12. Armentrout, P. B.; Shin, S.; Liyanage, R. Guided-Ion Beam and Theoretical Study of the Potential Energy Surface for Activation of Methane by W^+ *J. Phys. Chem. A* **2006,** *110*, 1242-1260.
13. Li, F.-X.; Zhang, X.-G.; Armentrout, P. B. The Most Reactive Third-row Transition Metal: Guided Ion Beam and Theoretical Studies of the Activation of Methane by Ir^+. *Int. J. Mass Spectrom.* **2006,** *255/256*, 279-300.
14. Parke, L. G.; Hinton, C. S.; Armentrout, P. B. Experimental and Theoretical Studies of the Activation of Methane by Ta^+ and the Bond Energies of Ta^+-CH_x (x = 1 - 3). *J. Phys. Chem. C* **2007,** *111*, 17773-17787.
15. Shayesteh, A.; Lavrov, V. V.; Koyanagi, G. K.; Bohme, D. K. Reactions of Atomic Cations with Methane: Gas Phase Room-Temperature Kinetics and Periodicities in Reactivity. *J. Phys. Chem. A* **2009,** *113*, 5602–5611.
16. Armentrout, P. B.; Parke, L.; Hinton, C.; Citir, M. Activation of Methane by Os^+: Guided Ion Beam and Theoretical Studies. *ChemPlusChem* **2013,** *78*, 1157-1173.
17. Armentrout, P. B. Methane Activation by 5d Transition Metals: Energetics, Mechanisms, and Periodic Trends. *Chem.: Eur. J.* **2017,** *23*, 10-18.
18. Lapoutre, V. J. F.; Redlich, B.; van der Meer, A. F. G.; Oomens, J.; Bakker, J. M.; Sweeney, A.; Mookherjee, A.; Armentrout, P. B. Structures of the Dehydrogenation Products of Methane Activation by 5d Transition Metal Cations. *J. Phys Chem. A* **2013,** *117*, 4115-4126.

19. Owen, C. J.; Boles, G. C.; Chernyy, V.; Bakker, J. M.; Armentrout, P. B. Structures of the Dehydrogenation Products of Methane Activation by 5d Transition Metal Cations Revisited: Deuterium Labeling and Rotational Contours. *J. Chem. Phys.* **2018,** *148*, 044307.
20. Bakker, J. M.; Owen, C. J.; Nooteboom, S. W.; Lushchikova, O. V.; Armentrout, P. B. Structural characterization of $[M,C,2H]^+$ products formed by reaction of 5d metal cations Pt^+ and Ir^+ with ethylene oxide and Ta^+ with methane using messenger spectroscopy. *J. Mol. Spectrosc.* **2021,** *378*, 111472.
21. Armentrout, P. B.; Kuijpers, S.; Lushchikova, O.; Hightower, R. L.; Boles, G. C.; Bakker, J. M. Spectroscopic Identification of the Carbyne Hydride Structure of the Dehydrogenation Product of Methane Activation by Osmium Cations. *J. Am. Soc. Mass Spectrom.* **2018,** *29*, 1781-1791.
22. Perry, J. K.; Ohanessian, G.; Goddard, W. A. Mechanism and Energetics for Dehydrogenation of Methane by Gaseous Iridium Ions. *Organomet.* **1994,** *13*, 1870-1877.
23. Halle, L. F.; Armentrout, P. B.; Beauchamp, J. L. Formation of Chromium Carbene Ions by Reaction of Electronically Excited Chromium Ions with Methane in the Gas Phase. *J. Am. Chem. Soc.* **1981,** *103*, 962-963.
24. Aristov, N.; Armentrout, P. B. Methane Activation by V^+: Electronic and Translational Energy Dependence. *J. Phys. Chem.* **1987,** *91*, 6178-6188.
25. Schultz, R. H.; Elkind, J. L.; Armentrout, P. B. Electronic Effects in C-H and C-C Bond Activation: State-specific Reactions of $Fe^+(^6D, ^4F)$ with Methane, Ethane and Propane. *J. Am. Chem. Soc.* **1988,** *110*, 411-423.
26. Sunderlin, L. S.; Armentrout, P. B. Methane Activation by Ti^+: Electronic and Translational Energy Dependence. *J. Phys. Chem.* **1988,** *92*, 1209-1219.
27. Georgiadis, R.; Armentrout, P. B. Translational and Electronic Energy Dependence of Chromium Ion Reactions with Methane. *J. Phys. Chem.* **1988,** *92*, 7067-7074.
28. Sunderlin, L. S.; Armentrout, P. B. Periodic Trends in Chemical Reactivity: Reactions of Sc^+, Y^+, La^+, and Lu^+ with Methane and Ethane. *J. Am. Chem. Soc.* **1989,** *111*, 3845-3855.
29. Georgiadis, R.; Armentrout, P. B. Translational and Electronic Energy Dependence of the Reaction of Mn^+ with Ethane. *Int. J. Mass Spectrom. Ion Process.* **1989,** *91*, 123-133.
30. Haynes, C. L.; Chen, Y.-M.; Armentrout, P. B. The Potential Energy Surface for Activation of Methane by Co^+: An Experimental Study. *J. Phys. Chem.* **1995,** *99*, 9110-9117.
31. Liu, F.; Zhang, X.-G.; Armentrout, P. B. Activation of CH_4 by Gas-phase Ni^+ and the Thermochemistry of Ni Ligand Complexes. *Phys. Chem. Chem. Phys.* **2005,** *7*, 1054-1064.
32. Ranasinghe, Y. A.; MacMahon, T. J.; Freiser, B. S. Formation of Thermodynamically Stable Dications in the Gas Phase by Thermal Ion-Molecule Reactions: Ta^{2+} and Zr^{2+} with Small Alkanes. *J. Phys. Chem* **1991,** *95*, 7721-7726.
33. Van Koppen, P. A. M.; Kemper, P. R.; Bushnell, J. E.; Bowers, M. T. Methane Dehydrogenation by Ti^+: A Cluster-Assisted Mechanism for σ-Bond Activation. *J. Am. Chem. Soc.* **1995,** *117*, 2098-2099.
34. Chen, Y.-M.; Armentrout, P. B. Activation of Methane by Gas-Phase Rh^+. *J. Phys. Chem.* **1995,** *99*, 10775-10779.
35. Chen, Y.-M.; Sievers, M. R.; Armentrout, P. B. Activation of CH_4, C_2H_6, C_3H_8, and c-C_3H_6 by Gas-phase Pd^+ and the Thermochemistry of Pd-ligand Complexes. *Int. J. Mass Spectrom. Ion Processes* **1997,** *167/168*, 195-212.

36. Sievers, M. R.; Chen, Y.-M.; Haynes, C. L.; Armentrout, P. B. Activation of CH_4, C_2H_6, and C_3H_8 by Gas-Phase Nb^+ and the Thermochemistry of Nb-ligand Complexes. *Int. J. Mass Spectrom.* **2000,** *195/196*, 149-170.
37. Armentrout, P. B.; Sievers, M. R. Activation of CH_4 by Gas-phase Zr^+ and the Thermochemistry of Zr ligand Complexes. *J. Phys. Chem. A* **2003,** *107*, 4396-4406.
38. Armentrout, P. B. Activation of CH_4 by Gas-phase Mo^+ and the Thermochemistry of Mo-ligand Complexes. *J. Phys. Chem. A* **2006,** *110*, 8327-8338.
39. Armentrout, P. B.; Chen, Y.-M. Activation of Methane by Ru^+: Experimental and Theoretical Studies of the Thermochemistry and Mechanism. *Int. J. Mass Spectrom.* **2016,** *413*, 135-149.
40. Armentrout, P. B.; Sunderlin, L. S.; Fisher, E. R. Intrinsic Transition Metal–Carbon Double Bond Dissociation Energies: Periodic Trends in M^+–CH_2 Bond Strengths. *Inorg. Chem.* **1989,** *28*, 4436-4437.
41. Armentrout, P. B.; Kickel, B. L., Gas-Phase Thermochemistry of Transition Metal Ligand Systems: Reassessment of Values and Periodic Trends. In *Organometallic Ion Chemistry*, Freiser, B. S., Ed. Kluwer: Dordrecht, 1996; pp 1-45.
42. Haynes, C. L.; Chen, Y.-M.; Armentrout, P. B. The Reaction of $FeCH_2^+ + D_2$: Probing the $[FeCH_4]^+$ Potential Energy Surface. *J. Phys. Chem.* **1996,** *100*, 111-119.
43. Husband, J.; Aguirre, F.; Thompson, C. J.; Laperle, C. M.; Metz, R. B. Photofragment Spectroscopy of $FeCH_2^+$, $CoCH_2^+$, and $NiCH_2^+$ near the M^+−CH_2 Dissociation Threshold. *J. Phys. Chem. A* **2000,** *104*, 2020-2024.
44. Ruscic, B.; Bross, D. H. Active Thermochemical Tables (ATcT) values based on ver. 1.124 of the Thermochemical Network. available at ATcT.anl.gov (accessed 10/18/22).
45. Villaume, S.; Strich, A.; Ndoye, C. A.; Daniel, C.; Perera, S. A.; Bartlett, R. J. Theoretical Study of the Electronic Structure of MCH_2^+(M=Fe,Co,Ni). *J. Chem. Phys.* **2007,** *126*, 154318.
46. Musaev, D. G.; Morokuma, K.; Koga, N.; Nguyen, K. A.; Gordon, M. S.; Cundari, T. R. Ab initio study of the molecular and electronic structure of $CoCH_2^+$ and of the reaction mechanism of $CoCH_2^+ + H_2$. *J. Phys. Chem.* **1993,** *97*, 11435-11444.
47. Musaev, D. G.; Morokuma, K. Ab initio molecular orbital study of the molecular and electronic structure of $FeCH_2^+$ and of the reaction mechanism of $FeCH_2^+ + H_2$. *J. Chem. Phys.* **1994,** *101*, 10697-10707.
48. Loh, S. K.; Fisher, E. R.; Lian, L.; Schultz, R. H.; Armentrout, P. B. State Specific Reactions of $Fe^+(^6D, ^4F)$ with O_2 and cyclo-C_2H_4O: $D^o_0(Fe^+\text{-}O)$ and Effects of Collisional Relaxation. *J. Phys. Chem* **1989,** *93*, 3159-3167.
49. Fisher, E. R.; Armentrout, P. B. Reactions of Co^+, Ni^+, and Cu^+ with Cyclopropane and Ethylene Oxide: Metal Methylidene Ion Bond Energies. *J. Phys. Chem.* **1990,** *94*, 1674-1683.
50. Wensink, F. J.; Roos, N.; Bakker, J. M.; Armentrout, P. B. C–H Bond Activation and C–C Coupling of Methane on a Single Cationic Platinum Center: A Spectroscopic and Theoretical Study. *Inorg. Chem.* **2022,** *61*, 11252-11260.
51. Wensink, F. J.; Smink, C. E.; Steele, R. P.; Armentrout, P. B.; Bakker, J. M. IR spectroscopic characterization of $[M,C,2H]^+$ (M = Ru and Rh) products formed by reacting 4d transition metal cations with oxirane: Spectroscopic evidence for multireference character in $RhCH_2^+$. *Phys. Chem. Chem. Phys.*, submitted for publication.
52. Wensink, F. J.; Münst, M. G.; Heller, J.; Ončák, M.; Bakker, J. M.; Van Der Linde, C. IR Multiple Photon Dissociation Spectroscopy of MO_2^+ (M = V, Nb, Ta). *J. Chem. Phys. 2020, 153 (17), 171101.* **2020,** *153*, 171101.

53. Berg, C.; Schindler, T.; Niedner-Schatteburg, G.; Bondybey, V. E. Reactions of Simple Hydrocarbons with Nb_n^+: Chemisorption and Physisorption on Ionized Niobium Clusters. *J. Chem. Phys.* **1995,** *102*, 4870-4884.
54. Marshall, A. G.; Hendrickson, C. L.; Jackson, G. S. Fourier Transform Ion Cyclotron Resonance Mass Spectrometry: A Primer. *Mass Spectrom. Rev.* **1998,** *17*, 1-35.
55. Frisch, M. J.; Trucks, G. W.; Schlegel, H. B.; Scuseria, G. E.; Robb, M. A.; Cheeseman, J. R.; Scalmani, G.; Barone, V.; Petersson, G. A.; Nakatsuji, H., et al. *Gaussian 16 Rev. C.01*, Wallingford, CT, 2016.
56. Becke, A. D. Density-functional Thermochemistry. III. The Role of Exact Exchange. *J. Chem. Phys.* **1993,** *98*, 5648-5652.
57. Lee, C.; Yang, W.; Parr, R. G. Development of the Colle-Salvetti Correlation-Energy Formula into a Functional of the Electron Density. *Phys. Rev. B* **1988,** *37*, 785-789.
58. Weigand, A.; Cao, X.; Hangele, T.; Dolg, M. Relativistic Small-Core Pseudopotentials for Actinium, Thorium, and Protactinium. *J. Phys. Chem. A* **2014,** *118*, 2519-2530.
59. Meerts, W. L.; Schmitt, M. Application of Genetic Algorithms in Automated Assignments of High-Resolution Spectra. *Int. Rev. Phys. Chem.* **2006,** *25*, 353-406.
60. Möller, C.; Plesset, M. S. Note on an Approximation Treatment for Many-Electron Systems. *Phys. Rev.* **1934,** *46*, 618-622.
61. Bartlett, R. J. Many-body Perturbation Theory and Coupled Cluster Theory for Electron Correlation in Molecules. *Ann. Rev. Phys. Chem.* **1981,** *32*, 359-401.
62. Armentrout, P. B.; Stevenson, B. C.; Yang, F.; Wensink, F. J.; Lushchikova, O. V.; Bakker, J. M. Infrared Spectroscopy of Gold Carbene Cation ($AuCH_2^+$): Covalent or Dative Bonding? *J. Phys. Chem. A* **2019,** *123*, 8932-8941.
63. Wheeler, O. W.; Salem, M.; Gao, A.; Bakker, J. M.; Armentrout, P. B. Sequential Activation of Methane by Ir^+: An IRMPD and Theoretical Investigation. *Int. J. Mass Spectrom.* **2019,** *435*, 78-92.
64. Wheeler, O. W.; Salem, M.; Gao, A.; Bakker, J. M.; Armentrout, P. B. Activation of C-H bonds in $Pt^+ + xCH_4$ Reactions, Where x = 1 – 4: Identification of the Platinum Dimethyl Cation. *J. Phys. Chem. A* **2016,** *120*, 6216–6227.
65. Zhang, Y.; Yang, W. A challenge for density functionals: Self-interaction error increases for systems with a noninteger number of electrons. *J. Chem. Phys.* **1998,** *109*, 2604-2608.
66. Lundberg, M.; Siegbahn, P. E. M. Quantifying the effects of the self-interaction error in DFT: When do the delocalized states appear? *J. Chem. Phys.* **2005,** *122*, 224103.
67. Hait, D.; Head-Gordon, M. Delocalization Errors in Density Functional Theory Are Essentially Quadratic in Fractional Occupation Number. *The Journal of Physical Chemistry Letters* **2018,** *9*, 6280-6288.
68. Bryenton, K. R.; Adeleke, A. A.; Dale, S. G.; Johnson, E. R. Delocalization error: The greatest outstanding challenge in density-functional theory. *WIREs Computational Molecular Science* **2023,** *13*, e1631.
69. Perdew, J. P.; Chevary, J. A.; Vosko, S. H.; Jackson, K. A.; Pederson, M. R.; Singh, D. J.; Fiolhais, C. Atoms, molecules, solids, and surfaces: Applications of the generalized gradient approximation for exchange and correlation. *Phys. Rev. B* **1992,** *46*, 6671-6687.
70. Perdew, J. P.; Burke, K.; Wang, Y. Generalized gradient approximation for the exchange-correlation hole of a many-electron system. *Phys. Rev. B* **1996,** *54*, 16533-16539.

71. Tao, J.; Perdew, J. P.; Staroverov, V. N.; Scuseria, G. E. Climbing the Density Functional Ladder: Nonempirical Meta--Generalized Gradient Approximation Designed for Molecules and Solids. *Phys. Rev. Lett.* **2003,** *91*, 146401.
72. Grimme, S.; Ehrlich, S.; Goerigk, L. Effect of the Damping Function in Dispersion Corrected Density Functional Theory. *J. Comput. Chem.* **2011,** *32*, 1456-1465.
73. Xu, X.; Goddard, W. A. The X3LYP extended density functional for accurate descriptions of nonbond interactions, spin states, and thermochemical properties. *Proc. Natl. Acad. Sci.* **2004,** *101*, 2673-2677.
74. Chai, J.-D.; Head-Gordon, M. Long-range corrected hybrid density functionals with damped atom–atom dispersion corrections. *Phys. Chem. Chem. Phys.* **2008,** *10*, 6615-6620.
75. Zhao, Y.; Truhlar, D. G. Density Functionals with Broad Applicability in Chemistry. *Acc. Chem. Res.* **2008,** *41*, 157.
76. Yanai, T.; Tew, D. P.; Handy, N. C. A new hybrid exchange–correlation functional using the Coulomb-attenuating method (CAM-B3LYP). *Chem. Phys. Lett.* **2004,** *393*, 51-57.
77. Yu, H. S.; He, X.; Truhlar, D. G. MN15-L: A New Local Exchange-Correlation Functional for Kohn–Sham Density Functional Theory with Broad Accuracy for Atoms, Molecules, and Solids. *J. Chem. Theory Comput.* **2016,** *12*, 1280-1293.
78. Adamo, C.; Barone, V. Toward reliable adiabatic connection models free from adjustable parameters. *Chem. Phys. Lett.* **1997,** *274*, 242-250.
79. Zhao, Y.; Truhlar, D. G. The M06 Suite of Density Functionals for Main Group Thermochemistry, Thermochemical Kinetics, Noncovalent Interactions, Excited States, and Transition Elements: Two New Functionals and Systematic Testing of Four M06-Class Functionals and 12 Other Functionals. *Theor. Chem. Acc.* **2008,** *120*, 215-241.
80. Brémond, E.; Adamo, C. Seeking for parameter-free double-hybrid functionals: The PBE0-DH model. *J. Chem. Phys.* **2011,** *135*, 024106.
81. Elkind, J. L.; Armentrout, P. B. State-specific Reactions of Atomic Transition Metal Ions with H_2, HD and D_2: Effects of d Orbitals on Chemistry. *J. Phys. Chem.* **1987,** *91*, 2037-2045.
82. Armentrout, P. B.; Chen, Y.-M. Activation of C_2H_6, C_3H_8, $HC(CH_3)_3$, and c-C_3H_6 by Gas-Phase Ru^+ and the Thermochemistry of Ru-ligand Complexes. *J. Am. Soc. Mass Spectrom.* **1999,** *10*, 821-839.
83. Armentrout, P. B.; Kretzschmar, I. Guided Ion Beam and Theoretical Studies of the Reaction of Ru^+ with CS_2 in the Gas-phase: Thermochemistry of RuC^+, RuS^+, and $RuCS^+$. *Phys. Chem. Chem. Phys.* **2010,** *12*, 4078-4091.
84. Hettich, R. L.; Freiser, B. S. Gas-Phase Photodissociation of $FeCH_2^+$ and $CoCH_2^+$: Determination of the Carbide, Carbyne, and Carbene Bond Energies. *J. Am. Chem. Soc.* **1986,** *108*, 2537–2540.
85. Kramida, A.; Ralchenko, Y.; Reader, J.; Team, N. A. NIST Atomic Spectra Database (ver. 5.7.1), [Online]. Available: http://physics.nist.gov/asd 2012. (accessed Nov 1, 2019).

Table 1: Fragmentation channels and dissociation energies (D_0) of the lowest energy $[M,C,2H]^+$ species.

Species	Fragments	Bond dissociation energy D_0 (eV)	
		Theory[a]	Experiment
$FeCH_2^+$	$FeC^+ + H_2$	3.30	2.86 ± 0.22 [b]
	$Fe^+ + CH_2$	3.66	3.56 ± 0.22,[b] 3.53 ± 0.04,[c] ≤3.54 ± 0.02 [d]
$CoCH_2^+$	$CoC^+ + H_2$	3.77	3.08 ± 0.22,[b] 3.01 ± 0.30,[c,e,f] ≤3.15 ± 0.30 [d,e,f]
	$Co^+ + CH_2$	3.24	3.64 ± 0.22,[b] 3.29 ± 0.05,[c] ≤3.43 ± 0.02 [d]

[a] Theoretical values are calculated at the uB3LYP/def2-TZVPPD level of theory. [b] Ref. [84]. [c] Ref. [41]. [d] Ref. [43]. [e] Ref. [30]. [f] Uses $D_0(C–H_2)$ = 3.320 ± 0.001 eV.[44]

Table 2: Experimental band positions and strengths (s=strong, m=medium, w=weak) accompanied by theoretical calculated frequencies, intensities, and descriptions for the assigned structures.

	Experiment		Theory B3LYP/CCSD[a]		
	Frequency (cm^{-1})	Strength	Frequency (cm^{-1})	Intensity (km/mol)	Mode description
$FeCH_2^+$ ($^4B_1$)			554/570	36/45	CH_2 rocking
	632	s	627/647	5/43	M–C stretch
	767	m	787/754	101/106	CH_2 wagging
	-	-	1321/1358	1/1	CH_2 scissor
$FeCH_2^+$ ($^4B_2$)			555/567	40/50	CH_2 rocking
	632	s	632/646	9/43	M–C stretch
	767	m	716/744	69/98	CH_2 wagging
	-	-	1319/1359	0/1	CH_2 scissor
$CoCH_2^+$ ($^3A_2$)			622/625	36/41	CH_2 rocking
	673	s	631/690	0/25	M–C stretch
	811	s	877/861	88/100	CH_2 wagging
	948	m	1377/1410	3/23	CH_2 scissor
$CoCH_2^+$ ($^3A_1$)			601/624	31/39	CH_2 rocking
	673	s	625/693	1/14	M–C stretch
	811	s	893/881	89/100	CH_2 wagging
	948	m	1382/1416	3/30	CH_2 scissor

[a] B3LYP and CCSD calculations used the def2-TZVPPD basis set.

Table 3: Predicted vibrational frequencies in cm^{-1} (intensities in km/mol) for $FeCH_2^+$ ($^4B_1$) calculated at multiple levels of theory.

Level of theory	CH_2 rock	Fe-C stretch	CH_2 wag	CH_2 scissors
TPSS[71]	509 (24)	619 (3)	808 (102)	1313 (0)
B3LYP[56, 57]	554 (36)	627 (5)	787 (101)	1321 (1)
B3LYP-GD3BJ[72]	555 (36)	627 (5)	787 (101)	1321 (1)
X3LYP[57, 73]	556 (37)	630 (6)	784 (101)	1321 (1)
ωB97X-D[74]	549 (44)	675 (7)	790 (109)	1345 (6)
PW6B95D3[75]	549 (40)	638 (8)	776 (104)	1327 (1)
B3PW91[56, 69, 70]	544 (36)	639 (9)	769 (103)	1307 (1)
Cam-B3LYP[76]	554 (42)	655 (10)	786 (107)	1335 (6)
MN15L[77]	449 (1.4)	632 (11)	770 (96)	1318 (<1)
PBE0[78]	548 (40)	645 (12)	754 (104)	1305 (<1)
M06-2X[79]	560 (48)	625 (16)	678 (83)	1311 (3)
BHHLYP[57]	586 (52)	648 (23)	728 (97)	1358 (3)
PBE0-DH[80]	635 (55)	654 (24)	802 (104)	1363 (1)
CCSD(full)[61]	570 (45)	647 (43)	754 (106)	1358 (1)
MP2(full)[60]	593 (47)	660 (76)	710 (81)	1409 (34)
MP2(full) – anharmonic	569 (44)	657 (88)	682 (82)	1432 (44)

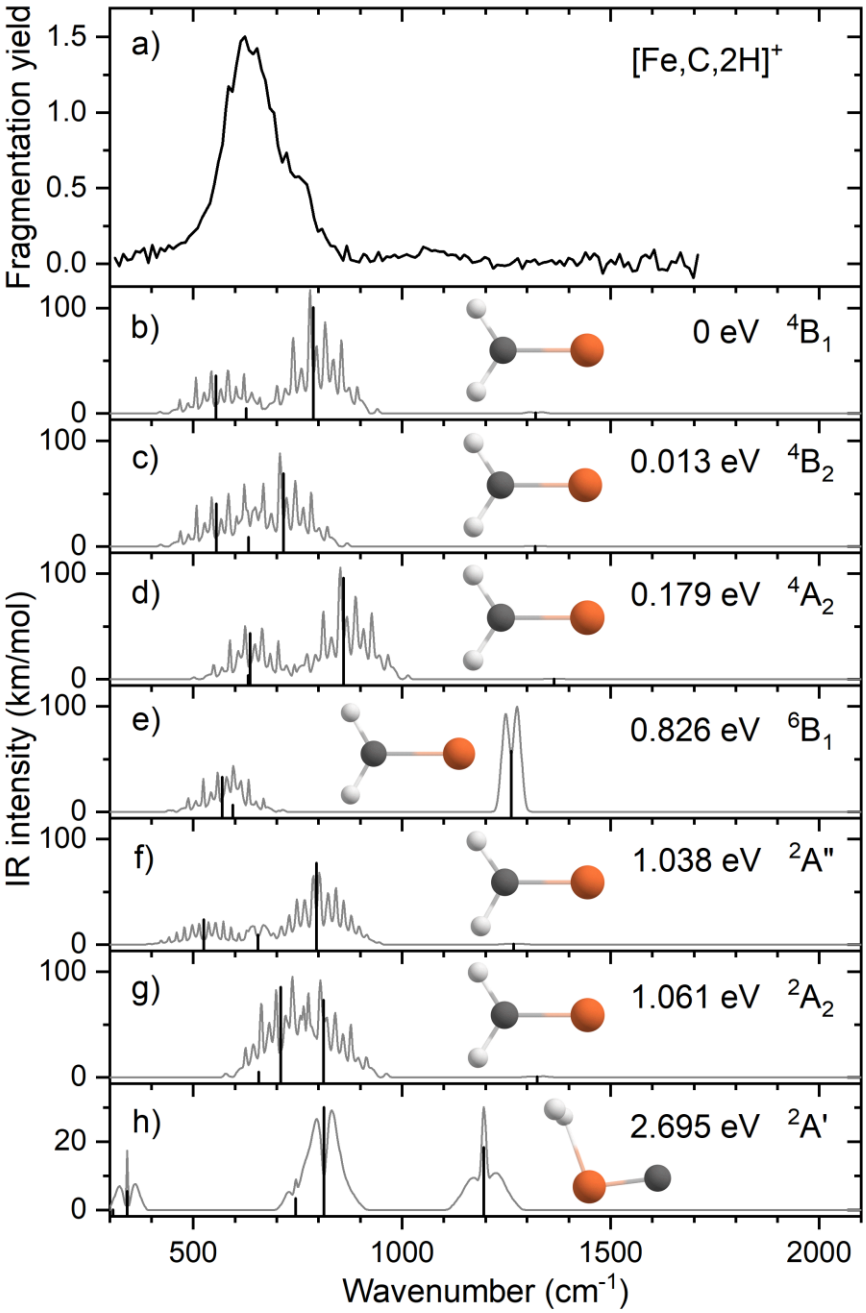

Figure 1: (a) Experimental IRMPD spectrum of $[Fe,C,2H]^+$; b-h) B3LYP/def2-TZVPPD calculated IR spectra of different $[Fe,C,2H]^+$ states and isomers with the harmonic vibrations in black and the rovibrational envelopes in grey accompanied by geometric structure, relative energy, and electronic state.

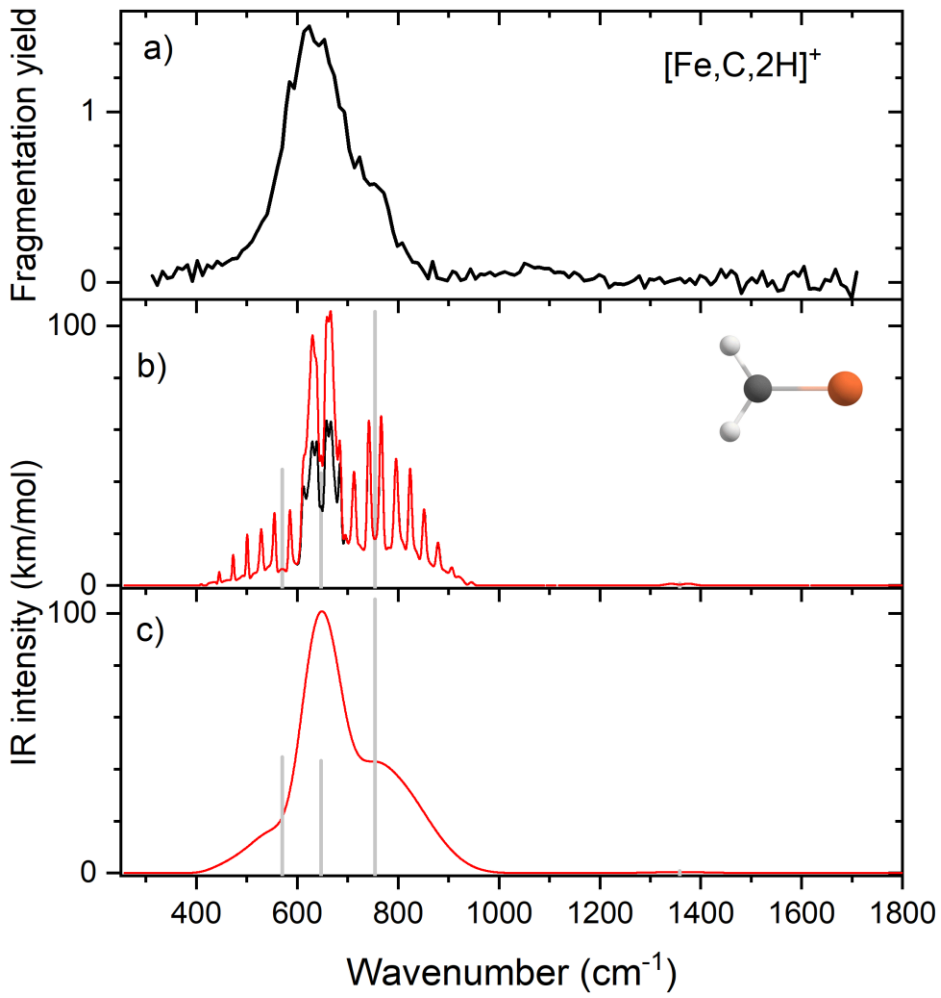

Figure 2: (a) Experimental IRMPD spectrum of $[Fe,C,2H]^+$; b) Harmonic stick spectrum of the $FeCH_2^+$ ($^4B_1$) structure at the CCSD/def2-TZVPPD level and rovibrational simulations using the original IR intensity for the Fe-C stretch mode at 43 km/mol (black) and with a double value (red); c) same as b) but convolved with a 9% FWHM Gaussian lineshape function to simulate broadening effects.

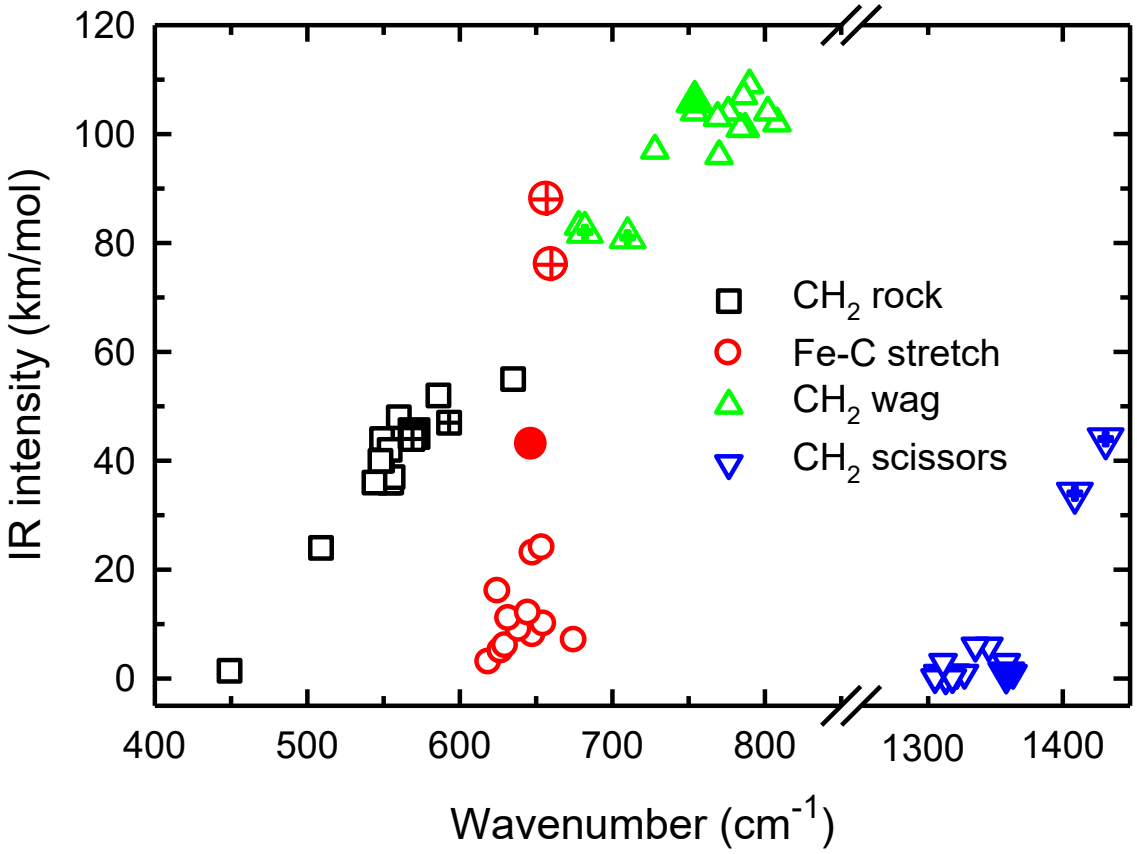

Figure 3: Theoretical IR intensities versus wavenumber for the four vibrations accessible experimentally in the present experiments. CCSD results are closed symbols and MP2 results are hatched.

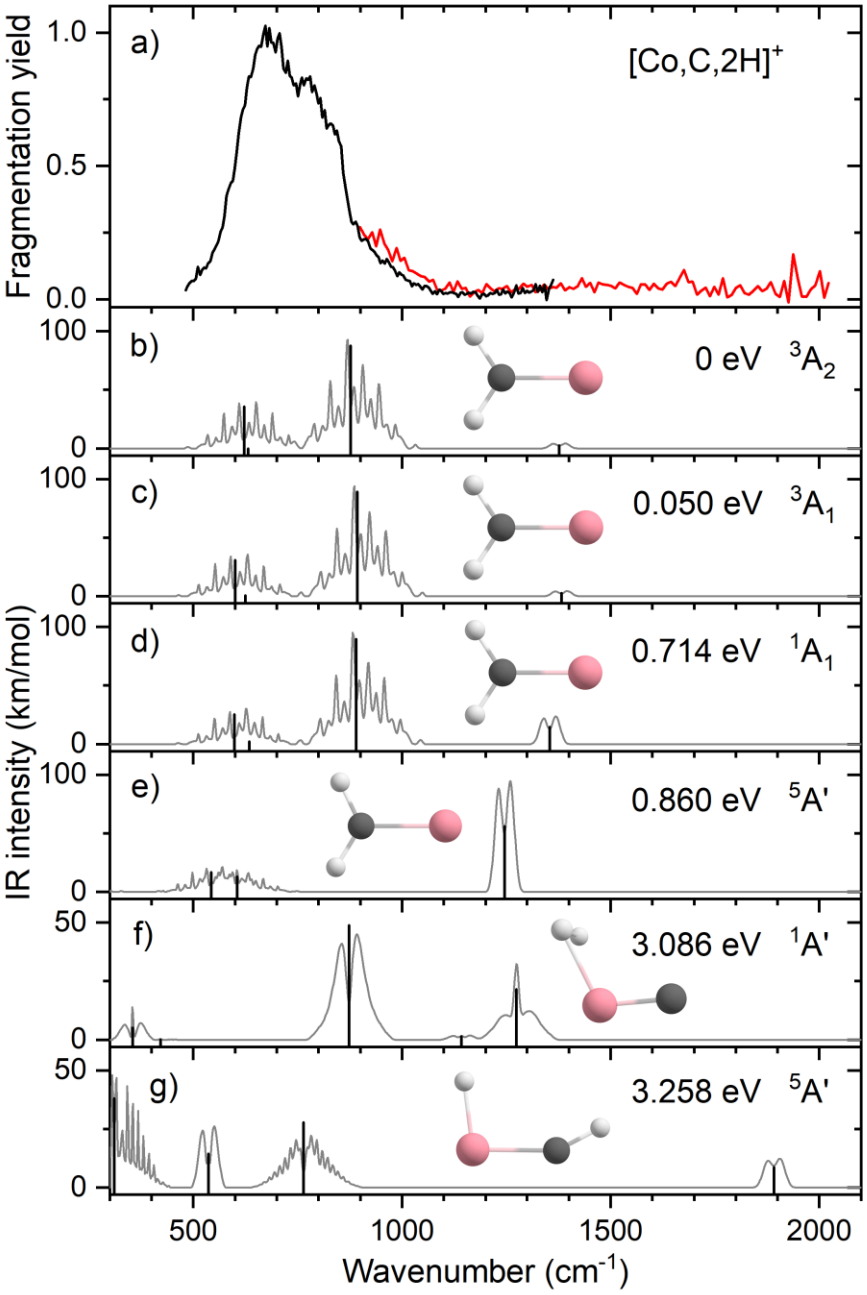

Figure 4: (a) Experimental IRMPD spectrum of $[Co,C,2H]^+$, the black trace is the average of two scans, the red trace is a single scan; b-g) B3LYP/def2-TZVPPD calculated IR spectra of different $[Co,C,2H]^+$ states and isomers with the harmonic vibrations in black and the rovibrational envelopes in grey accompanied by geometric structure, relative energy, and electronic state.

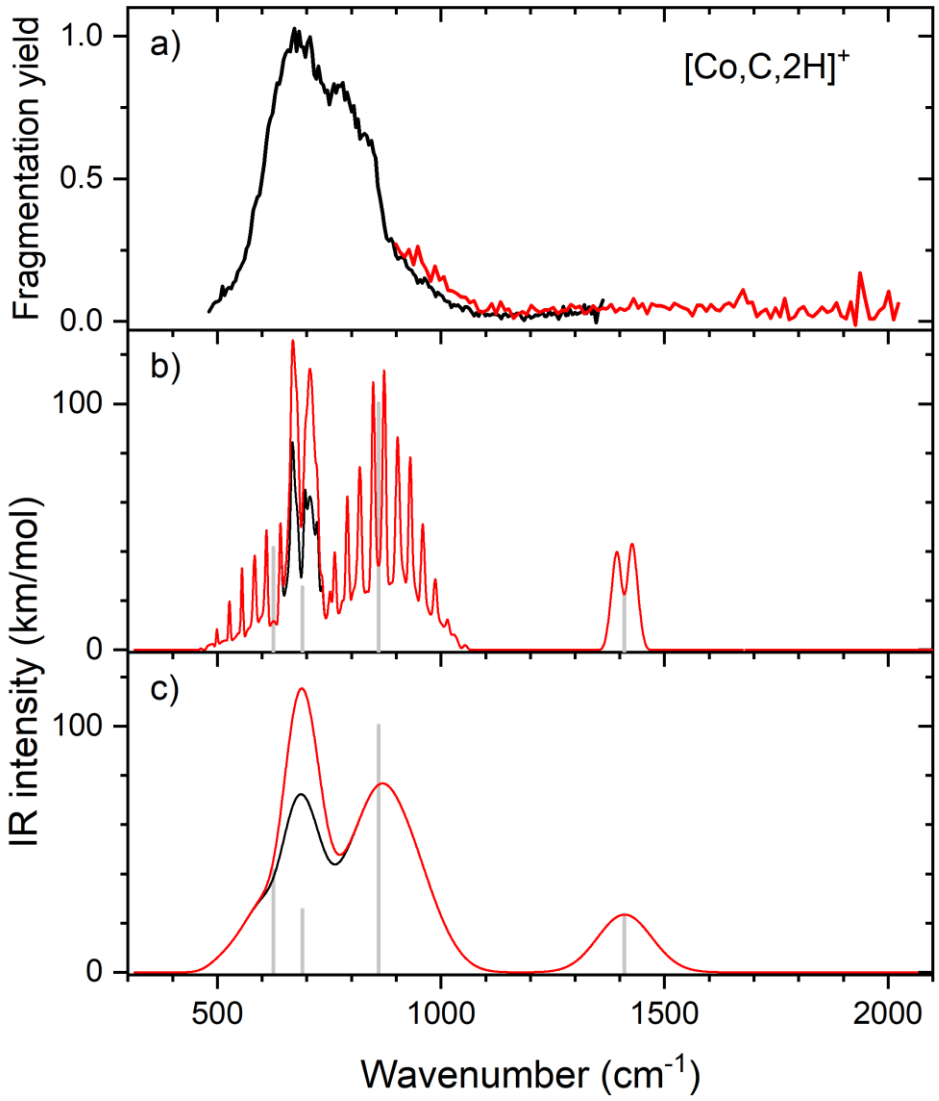

Figure 5: (a) Experimental IRMPD spectrum of $[Co,C,2H]^+$; b) Harmonic stick spectrum of the $CoCH_2^+$ ($^3A_2$) structure at the CCSD/def2-TZVPPD level and rovibrational simulations using the original IR intensity for the Co-C stretch mode at 25 km/mol (black) and with a double value (red); c) same as b) but convolved with a 9% FWHM Gaussian lineshape function to simulate broadening effects.

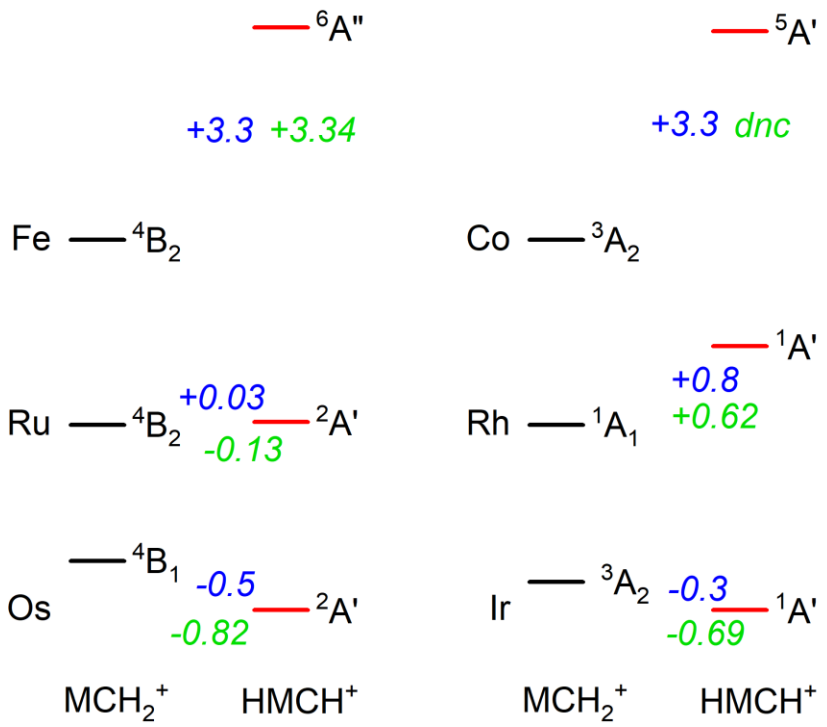

Figure 6: Energetic comparison between the lowest energy species of carbene (MCH_2^+) and hydrido carbyne ($HMCH^+$) structures for group 8 and 9 metal cations. For each, the lowest energy state of both configurations is indicated together with the energy difference, $E(HMCH^+) - E(MCH_2^+)$, in eV. B3LYP energetics for Os are taken from refs. [16, 21] and for Ir from ref. [18]; the other values are from this work. B3LYP/def2-TZVPPD energies are shown in blue and CCSD(T)//CCSD energies are in green. CCSD calculations for $HCoCH^+$ on the quintet spin surface did not converge (dnc).

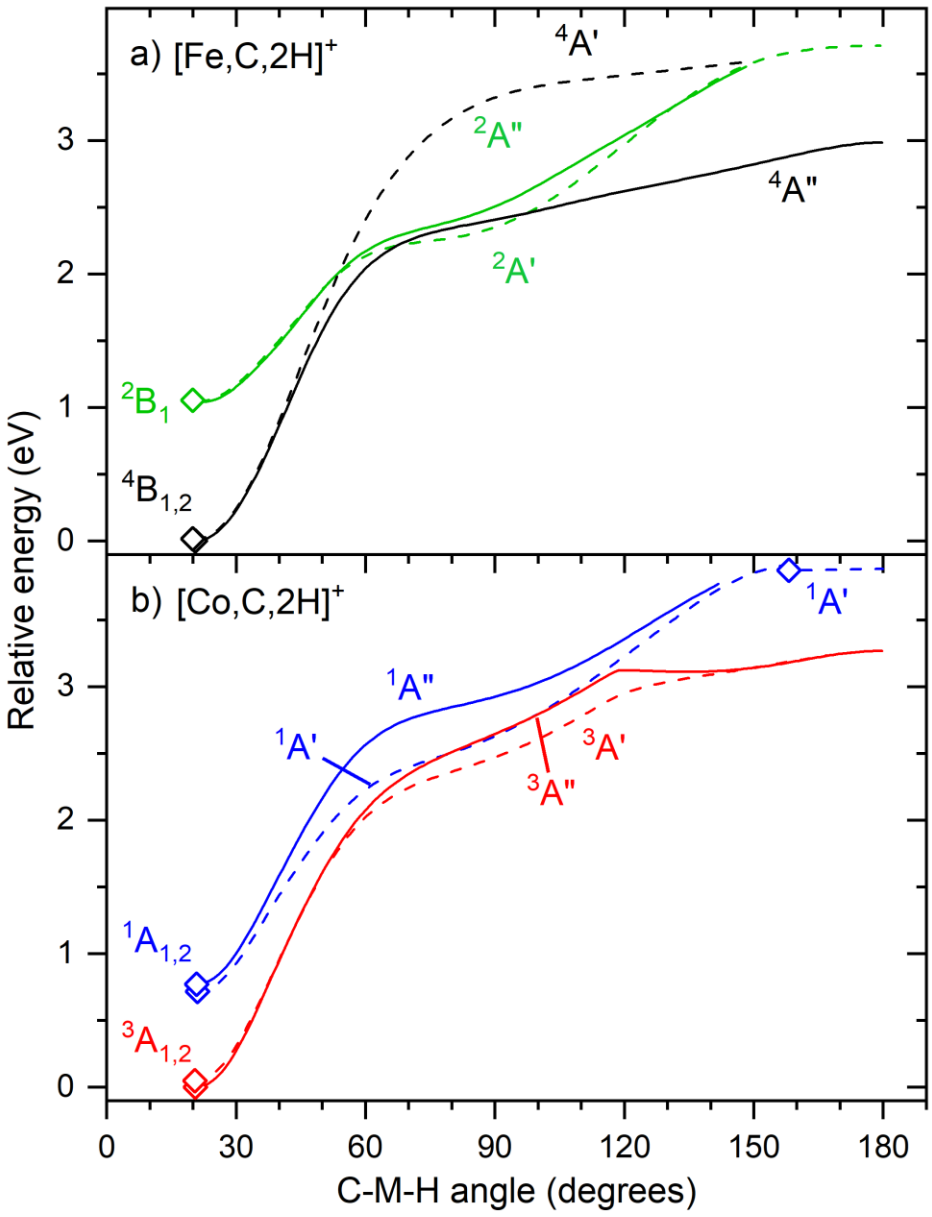

Figure 7: Potential energy surfaces of $[M,C,2H]^+$ along the C–M–H angle calculated at the uB3LYP/def2-TZVPPD level of theory. Solid diamonds indicate calculated structures that successfully converged to true minima at the indicated C–M–H angle. Solid lines indicate A" states while A' states are indicated by dashed lines. The doublet spin surface is depicted in green, quartet in black, singlet in blue and triplet in red. All energy values are relative to the GS symmetric carbene structures.